Draft version May 5, 2020
Typeset using LaTeX **twocolumn** style in AASTeX62

The big sibling of AU Mic: a cold dust-rich debris disk around CP−72 2713 in the β Pic moving group

Attila Moór,[1,2] Nicole Pawellek,[3,4,1] Péter Ábrahám,[1,2] Ágnes Kóspál,[1,4,2] Krisztián Vida,[1,2] András Pál,[1,2] Anne Dutrey,[5] Emmanuel Di Folco,[5] A. Meredith Hughes,[6] Quentin Kral,[7] and Ilaria Pascucci[8]

[1]*Konkoly Observatory, Research Centre for Astronomy and Earth Sciences, Konkoly-Thege Miklós út 15-17, H-1121 Budapest, Hungary*
[2]*ELTE Eötvös Loránd University, Institute of Physics, Pázmány Péter sétány 1/A, 1117 Budapest, Hungary*
[3]*Institute of Astronomy, University of Cambridge, Madingley Road, Cambridge CB3 0HA, UK*
[4]*Max Planck Institute for Astronomy, Königstuhl 17, D-69117 Heidelberg, Germany*
[5]*Laboratoire d'Astrophysique de Bordeaux, Univ. Bordeaux, CNRS, B18N, Allée Geoffroy Saint-Hilaire, F-33615 Pessac, France*
[6]*Department of Astronomy, Van Vleck Observatory, Wesleyan University, 96 Foss Hill Drive, Middletown, CT 06459, USA*
[7]*LESIA, Observatoire de Paris, Université PSL, CNRS, Sorbonne Université, Univ. Paris Diderot, Sorbonne Paris Cité, 5 place Jules Janssen, F-92195 Meudon, France*
[8]*Lunar and Planetary Laboratory, The University of Arizona, Tucson, AZ 85721, USA*

(Received date; Revised date; Accepted date)

Submitted to AJ

ABSTRACT

Analyzing *Spitzer* and *Herschel* archival measurements we identified a hitherto unknown debris disk around the young K7/M0 star CP−72 2713. The system belongs to the 24 Myr old β Pic moving group. Our new 1.33 mm continuum observation, obtained with the ALMA 7-m array, revealed an extended dust disk with a peak radius of 140 au, probably tracing the location of the planetesimal belt in the system. The disk is outstandingly large compared to known spatially resolved debris disks and also to protoplanetary disks around stars of comparable masses. The dynamical excitation of the belt at this radius is found to be reconcilable with planetary stirring, while self-stirring by large planetesimals embedded in the belt can work only if these bodies form very rapidly, e.g. via pebble concentration. By analyzing the spectral energy distribution we derived a characteristic dust temperature of 43 K and a fractional luminosity of 1.1×10^{-3}. The latter value is prominently high, we know only four other similarly dust-rich Kuiper-belt analogs within 40 pc of the Sun.

Keywords: Circumstellar disks(235); Debris disks(363); Late-type dwarf stars(906)

1. INTRODUCTION

Following the dispersal of their gas-rich primordial disks, typically by ∼10 Myr (e.g. Ercolano & Pascucci 2017), young stars are thought to be surrounded by planetesimals not incorporated into planets. Depending on the local level of dynamical excitation, in certain regions of the circumstellar environment low-velocity collisions between planetesimals can result in mergers, while in more stirred regions fragmentation can occur (Wyatt 2008). Second generation debris dust grains, produced in the emerging collisional cascade (Hughes et al. 2018), then make the sufficiently stirred parts of the disk observable through their thermal emission at infrared (IR) and millimeter wavelengths, and in optical/near-IR scattered light. Studying the spatial distribution of debris material can thus reveal regions where planetesimals could form but where the buildup of planets was halted by some environmental conditions.

Knowledge about the location of dust producing planetesimal belts in young systems can also allow us to constrain our models on the possible dynamical excitation mechanisms (Mustill & Wyatt 2009) as well as pinpointing how these belts form (Matrà et al. 2018). Further, the last few years have seen the discovery of an increasing number of young debris disks with detectable amount of gas material (e.g. Moór et al. 2011;

Corresponding author: Attila Moór
moor@konkoly.hu

Lieman-Sifry et al. 2016). In most cases this gas is likely second generation (Kral et al. 2019), originated from erosional processes. It implies the presence of volatile-rich bodies (Kral et al. 2017), thus allowing us to probe the ice abundances of (exo-)planetesimals (Kral et al. 2016; Matrà et al. 2017b; Matrà et al. 2019).

A significant fraction of the known young stars (10–50 Myr) in our neighbourhood belong to gravitationally unbound, loose associations of stars called moving groups (Torres et al. 2008). Previous IR observations obtained with spaceborne telescopes led to the discovery of many debris disks, including some of the most iconic ones (e.g. β Pic, AU Mic, Aumann 1985; Mathioudakis, & Doyle 1991), around the members of these kinematic assemblages (e.g. Rebull et al. 2008; Zuckerman et al. 2011; Donaldson et al. 2012; Riviere-Marichalar et al. 2014; Moór et al. 2016). These studies typically revealed higher excess detection rates in moving groups than in samples of older field stars which contain on average less dust as a result of longer collisional evolution of their planetesimal belts. This is particularly noticeable for debris disks around stars with spectral types later than K5, where the majority of the small number of known systems are harbored by moving group members (e.g., Kalas et al. 2004; Low et al. 2005; Olofsson et al. 2018; Flaherty et al. 2019; Sissa et al. 2018; Zuckerman 2019). Though the detection rate for debris disks with late type hosts is higher in young groups than among field stars, it is probable that the IR excess of several late-type members have remained undetected because their disks are faint due to the low luminosity of the host stars and/or their smaller disk masses in average.

By carefully inspecting the archives of far-infrared observations obtained by the *Spitzer Space Telescope* and the *Herschel Space Observatory*, we discovered a hitherto unknown cold, dust-rich debris disk around a nearby star CP−72 2713 (36.62±0.03 pc, Gaia Collaboration et al. 2018; Lindegren et al. 2018; Bailer-Jones et al. 2018). The star is late-type, Torres et al. (2006) derived a spectral type of K7e V from a high resolution spectrum, while Pecaut & Mamajek (2013) and Gaidos et al. (2014) obtained spectral types of K7e IV and M0, respectively, based on low resolution spectra. As a member of the ∼24 Myr old β Pic moving group (BPMG, Torres et al. 2006; Bell et al. 2015; Lee & Song 2018; Gagné et al. 2018), this disk provides a rare opportunity to study the early evolution of planetesimal belts surrounding late type stars.

In this paper we announce the discovery and present the first detailed analysis of this system by using multiwavelength observations. Based on spatially resolved far-IR *Herschel*/PACS and millimeter ALMA images of the dust emission, we model the structure of the disk and constrain the location of the dust producing planetesimal belt. Additionaly, we carried out ALMA line observations to look for CO molecules in the disk.

2. OBSERVATIONS AND DATA REDUCTION

2.1. *Spitzer/MIPS*

CP−72 713 was observed with the Multiband Imaging Photometer for Spitzer (MIPS, Rieke et al. 2004) on-board the Spitzer Space Telescope (Werner et al. 2004) at 24μm and 70μm on 2008 November 23 (PI: P. Plavchan). Photometry at 24μm was taken from the Spitzer Enhanced Imaging Products (SEIP) catalog. The photometric uncertainty was computed as the quadratic sum of the instrumental noise listed by the catalog and the calibration error of 4% (MIPS Instrument Handbook[1]). The SEIP catalog does not include data from the 70μm channel. Therefore, we downloaded the pipeline reduced Basic Calibrated Data images (version S18.13.0) from the Spitzer Heritage Archive and used MOPEX (MOsaicking and Point source Extraction, Makovoz & Marleau 2005) to co-add them and to correct for array distortions. For further improvement prior to the co-addition we applied column mean subtraction and time filtering for the images following Gordon et al. (2007). The final image shows a point source close to the Gaia DR2 position of CP−72 2713 (corrected for proper motion between the epochs of observations). The separation is only 0.″9 ($\Delta RA = -0.''86 \pm 0.''60$, $\Delta DEC = +0.''16 \pm 0.''60$), that is within the 1$\sigma$ uncertainty (1.″7) of the pointing reconstruction at 70μm (MIPS Instrument Handbook). It is somewhat smaller than the typical angular offsets measured by Carpenter et al. (2008, see their fig. 5) and Moór et al. (2011, fig. 3) in MIPS 70μm observations of debris disks with similar or higher signal-to-noise ratios (SNR>25). Therefore, it can be concluded that the observed emission matches well the position of our target.

We performed aperture photometry for this source with a radius of 16″, and sky annulus between 39″ and 65″. We applied the proper aperture correction factor and adopted a calibration error of 7% (MIPS Instrument Handbook) that was added quadratically to the measured uncertainty. The MIPS flux densities are given in Table 1.

2.2. *Herschel/PACS Observations*

We processed far-infrared imaging observations of CP−72 2713 carried out with the Photodetector Array

[1] https://irsa.ipac.caltech.edu/data/SPITZER/docs/mips/mipsinstrumentha

Camera and Spectrometer (PACS, Poglitsch et al. 2010) instrument of the *Herschel Space Observatory* on 2013 April 23 (PI: A. Tanner). These measurements were performed in mini scan-map mode (PACS Observer's Manual v2.5.13) at 100 and 160μm. The data reduction and calibration were done in the Herschel Interactive Processing Environment (HIPE, Ott 2010) version 14.2 using the standard pipeline script optimized for mini scan-map observations and applying the PACS calibration tree No. 78. To mitigate the low-frequency (1/f) noise present in the data we applied highpass filtering with filter width parameters of 20 and 35 at 100 and 160μm, respectively. Since this process introduces flux loss, the immediate vicinity of the target was excluded from the filtering using a 25″ radius circular mask positioned at the source's location. The final images were generated with pixel sizes of 1″ at 100μm and 2″ at 160μm.

CP−72 2713 was clearly detected in both PACS bands. The 100μm image is displayed in Fig. 1a. The positional offsets between the source's centroid and its proper motion corrected Gaia DR2 position is 1.″4 ($\Delta RA = -1.''06 \pm 0.''07$, $\Delta DEC = -0.''84 \pm 0.''07$) and 1.″6 ($\Delta RA = -1.''35 \pm 0.''20$, $\Delta DEC = -0.''76 \pm 0.''20$) at 100$\mu$m and 160$\mu$m, respectively. Sánchez-Portal et al. (2014) derived a typical absolute pointing accuracy of 0.″9 for the phase of the *Herschel* mission when our target's observations were performed. Utilizing large number of PACS mini scan-maps of standard stars, Marton et al. (2017) [2] found a median positional difference of 1.″5 for the blue PACS detector (70μm and 100μm filters) and 1.″7 for the red PACS detector (160μm). Our measured offsets correspond well to the latter values implying its instrumental origin.

We measured the source's flux by placing a 15″ radius aperture onto the centroid position, and a sky annulus between 60″ and 70″. Aperture corrections were taken from the appropriate calibration files. To estimate the uncertainty of the measured flux densities we placed sixteen apertures with radii identical to the source aperture evenly along the sky annulus and carried out photometry without background subtraction in each of them. Then the uncertainty was derived as the standard deviation of these background flux values. The final photometric uncertainty was calculated as a quadratic sum of this and the absolute calibrational uncertainty of the PACS detector (7%, Balog et al. 2014). The resulting flux densities are in Table 1.

[2] http://archives.esac.esa.int/hsa/legacy/HPDP/PACS/PACS-P/PPSC/HPPSC_Explanatory_Supplement_v2.2.pdf

To evaluate whether the detected source is spatially extended we fitted a 2-dimensional Gaussian model to the images using the `mpfit2dpeak` IDL procedure (Markwardt 2009). At 100μm the best fit Gaussian has a Full Width at Half Maximum (FWHM) of $8.''5 \pm 0.''3 \times 8.''1 \pm 0.''3$, while the FWHM sizes of the point spread function (PSF) in maps performed with scan speed of 20″/s (as in our case) are $6.''89 \times 6.''69$ (PACS Observer's Manual). This implies that CP−72 2713 is marginally resolved at 100μm. The fitted Gaussian at 160μm is consistent with the PSF.

Assuming that the observed emission arises from a circumstellar dust ring, we fitted a grid of simple disk models to the 100μm image. The models have three free parameters: the radius of the ring (R), the position angle (PA, measured east of north), and the inclination (i, angle of the disk plane with respect to the sky plane). Considering that the observation does not resolve the radial structure we assumed a Gaussian radial surface brightness profile that peaks at R and has an FWHM fixed to $0.2R$. Since at this wavelength the stellar photosphere is predicted to be $\sim$100× fainter than the measured flux density (Sect. 3) we neglected its contribution in our modelling. Disk images constructed in this way were then convolved with a PSF model that we constructed from mini-scan map observations of α Boo (OBS ID 1342247702/1342247703), processed in the same way as that of our target. The wings of the PACS beam forms a characteristic tri-lobe pattern whose orientation depends on the actual roll angle of the observation. To allow direct comparison, we rotated the image of α Boo to match the telescope's roll angle at the observation of CP−72 2713. In order to select the best-fitting model and estimate uncertainties of the fitted parameters, we used Bayesian inference following Moór et al. (2015). The best-fitting model parameters are: $R = 2.''7^{+0.''7}_{-0.''6}$ (or 99^{+22}_{-26} au), $i = 29^{\circ}{}^{+26^{\circ}}_{-21^{\circ}}$, $PA = 153^{\circ}{}^{+60^{\circ}}_{-64^{\circ}}$. This model and the residuals are displayed in Figure 1b-c. As Fig. 1c shows, toward the source no residuals higher than 3σ were observed. The $>3\sigma$ residuals at the edge of the displayed image are at angular separation >15″, and may be related to background sources.

2.3. *Observations with the ALMA 7-m Array*

We observed CP−72 2713 with the ALMA 7-m array in the framework of a Cycle 4 project (2016.2.00200.S, PI: Á. Kóspál) that focused on the gas content of young dust-rich debris disks. Our Band 6 observations include two 1.875 GHz wide continuum spectral windows each with 128 channels centered at 217.0 and 233.5 GHz and two additional windows that were designed to cover the

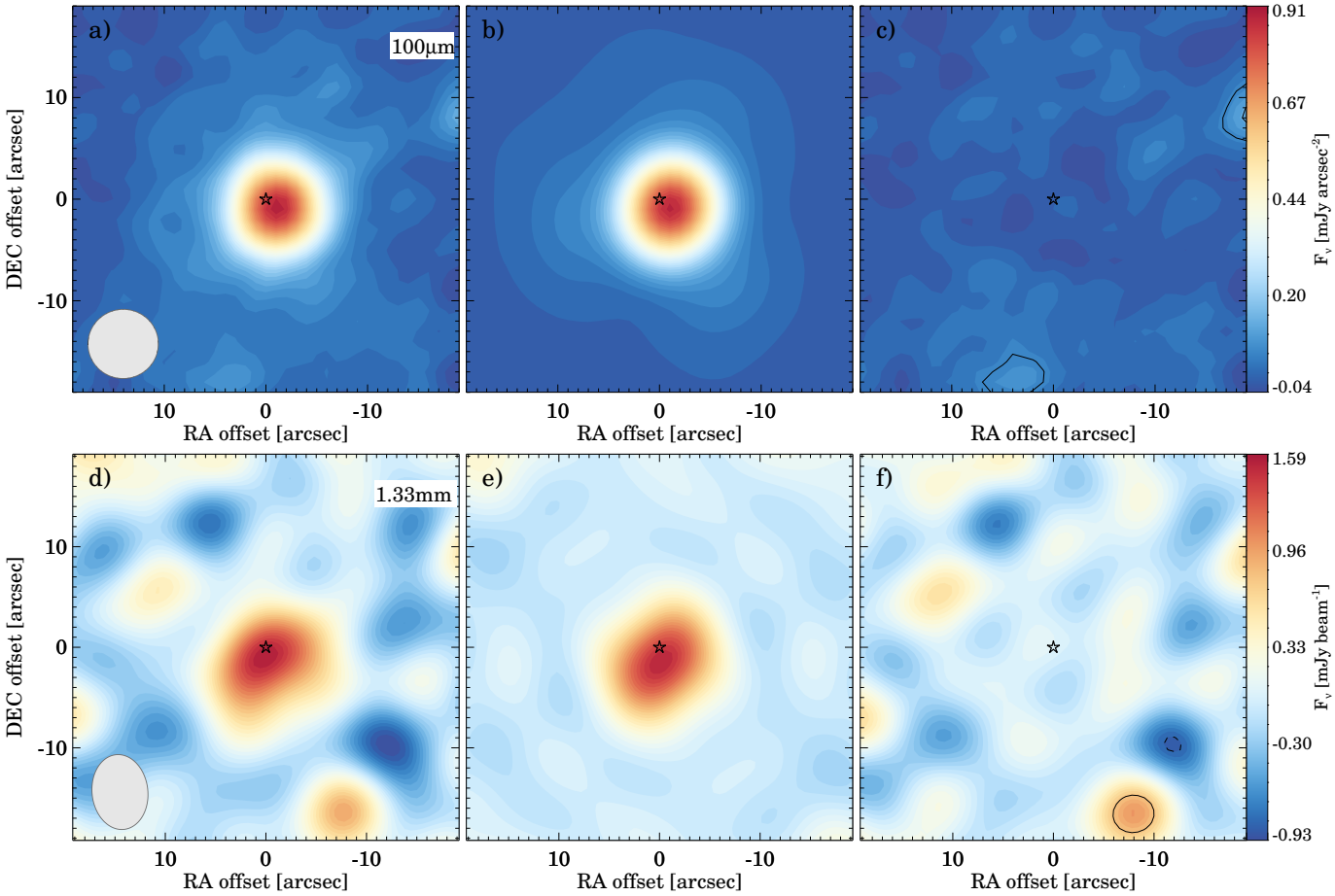

Figure 1. Upper panels: (a) PACS 100μm image of CP−72 2713, (b) simulated image of the best fit dust ring model convolved with our PACS PSF (see Sect 2.2), (c) the image of residuals. The stellar position is marked with a black star symbol. The gray filled ellipse in the lower-left corner represents the size and shape of the PACS PSF (the FWHMs and position angle of the ellipse were obtained by fitting a 2-dimensional Gaussian to the 100μm image of α Boo, see Sect. 2). In the residual image, contours of 3× the rms noise are also shown. Lower panels: (d) 1.33 mm ALMA continuum image, (e) image of the best-fit model, and (f) the residuals image. We note that our modelling was performed in the uv space (Sect. 2). The (e) and (f) panels display CLEAN images of the best-fit model and residuals after subtracting the model visibilities from the ALMA observations using Briggs weighting with a robustness parameter of 0.5 in the imaging. In the (f) panel the dashed and solid contours correspond to the -3σ and $+3\sigma$ levels.

J = 2–1 rotational lines of ^{12}CO, ^{13}CO, and C^{18}O. The latter two lines were measured in a single window using a channel width of 428.28 kHz and thereby providing a bandwidth of 1.875 GHz with 4096 channels. In the case of ^{12}CO the channel width was set to 122.07 kHz, this band had a total width of 468.8 MHz. Two observations were performed, one day apart from each other, on 2017 July 25 and 26. In both cases nine antennas were involved providing projected baseline lengths ranging between 8.9 and 44.7 m (6.7–33.6 kλ). The obtained data were calibrated and flagged with the ALMA reduction tool *Common Astronomy Software Applications* (CASA v4.7.2; McMullin et al. 2007) utilising the pipeline script delivered with the data.

Continuum emission—We used the `tclean` task in CASA (v5.6.2, McMullin et al. 2007) to construct the continuum image by applying Briggs weighting with a robustness parameter of 0.5. Since no line was detected (see below) we combined non-flagged data from all spectral windows achieving an rms noise level of 0.28mJy beam^{-1}. The beam size is $7\farcs4\times5\farcs5$ with a position angle of $6\fdg3$. The obtained 1.33 mm continuum image (Figure 1d) shows a moderately resolved source around CP−72 2713 with a peak signal-to-noise ratio (SNR) of 5.7. To determine the source's flux density and to constrain the spatial distribution of emitting dust grains we used the CASA-based `uvmultifit` tool (Martí-Vidal et al. 2014) that allows to fit models to the measured visibilities. Prior to this running, the data

weights were recomputed using the `statwt` task. Similarly to the case of PACS image analysis, we adopted a Gaussian ring model with a fixed FWHM width of $0.2R$. The obtained best-fit solution has $R = 140\pm14$ au ($3\farcs8\pm0\farcs4$), $i = 46° \pm 12°$, $PA = 130° \pm 16°$ and yields a flux density of 3.8±0.6 mJy (the quoted uncertainty includes 10% calibration uncertainty). We used the `tclean` task to compile images of the best-fit model and the residuals (Figure 1e-f). No significant residual emission appears in the disk region. The fitted center of the model ring shows an offset of $1\farcs3$ from the stellar position ($\Delta RA = -0\farcs3 \pm 0\farcs42$, $\Delta DEC = -1\farcs22 \pm 0\farcs45$). The positional accuracy of an ALMA observation with normal calibration can be estimated as the ratio of the achieved resolution and SNR, i.e. $\sim0\farcs9$ in our case, thus the observed offset is not significant. The best-fitting disk parameters derived from the analysis of PACS and ALMA data are summarized in Table 2.

Table 1. Measured continuum fluxes and predicted photospheric fluxes for CP−72 2713

λ (μm)	Meas. flux[a] (mJy)	Instrument	Photosph. flux (mJy)	Reference
9.00	128.1±12.3	IRC	105.2	Ishihara et al. (2010)
11.56	60.0±2.8	WISE	65.0	Cutri & et al. (2013)
22.09	18.9±1.5	WISE	18.3	Cutri & et al. (2013)
23.68	16.1±0.6	MIPS	16.0	SEIP
71.42	71.1±5.6	MIPS	1.8	This work
100[b]	110.6±9.7	PACS	0.9	This work
160	103.9±16.9	PACS	0.35	This work
1330[b]	3.80±0.59	ALMA	0.005	This work
8820	0.096±0.023	ATCA	10.6×10^{-5}	Brodie et al. in prep.

[a] The quoted flux densities are not color corrected.

[b] The emission is marginally resolved at these wavelengths.

CO line data—We used CASA to compile the spectral line cubes. After the continuum emission was subtracted from the calibrated visibilities using the `uvcontsub` task, the imaging was done with the `tclean` task. In the latter step we used Briggs weighting with a robustness parameter of 0.5 and the channel width was set to 0.4 km s^{-1} for the ^{12}CO line and to 1.4 km s^{-1} for data of the rarer ^{13}CO and C^{18}O isotopologues. Using the radial velocity data from Table 3 we derived a radial velocity of +0.4 km s^{-1} for CP−72 2713 in the LSR frame. We found no significant emission at this velocity (and nowhere else) in the CO data cubes.

In order to estimate an upper limit for the ^{12}CO (2–1) integrated line flux we assumed that the possible CO gas is co-located with the dust material in the disk. We defined a disk mask considering those regions in the millimeter continuum image that are adjacent with the maximum brightness and having SNR>2. Using the obtained mask we constructed the spectrum and calculated its rms. To consider the correlation between the neighboring channels due to the applied weighting function, this rms was multiplied by $\sqrt{2.667}$ (see Matrà et al. 2019, and references therein). Since based on our results the bulk of the dust is located at radii $\gtrsim$100 au and the disk inclination is $\lesssim$82° (3σ confidence interval), adopting a stellar mass of 0.71 $M_\odot$ (see Sect. 3.1) we expect a maximum line width of 5 km s^{-1}. Using the corrected rms value and this linewidth we derived a 3σ upper limit of 0.216 Jy km s^{-1} for the ^{12}CO (2–1) integrated line flux.

Table 2. Best-fitting dust disk parameters derived from the analysis of PACS and ALMA data

Data set	PA (°)	i (°)	R (au)
PACS 100μm	153^{+60}_{-64}	29^{+26}_{-21}	99^{+22}_{-26}
ALMA 1.33 mm	130±16	46±12	140±14

3. RESULTS AND ANALYSIS

3.1. *Basic stellar properties of CP−72 2713*

To estimate the basic stellar parameters of CP−72 2713 and provide photospheric flux predictions at infrared and millimeter wavelengths, we modeled the stellar photosphere by fitting an ATLAS9 atmosphere model (Castelli & Kurucz 2004) to the photometric data of the star. CP−72 2713 is an active star that exhibits variability due to spots (see Fig. 7). Using photometric data from the ASAS survey, Kiraga (2012) analysed 498 and 191 measurements in the V and I band, respectively. They derived average magnitudes and inferred variability amplitudes of 0.16 and 0.017 mag in the V and I bands. We derived an amplitude of ∼0.04 magnitude in the TESS band (Appendix A). To reduce uncertainties stemming from the spot-induced variability in the optical regime, we limited our analysis to data that are based on longer term monitoring observations taken from Kiraga (2012). This was further supplemented by near-IR (J, H, K_s) photometry from the Two Micron All-Sky Survey (2MASS, Skrutskie et al. 2006), and by $W1$, $W2$ band data from the AllWISE (Cutri & et al. 2013) catalog. These longer wavelength photometry are typically less susceptible to variations caused by spots (e.g., Goulding et al. 2012). Based on the recent 3D

reddening map of the local interstellar medium, that is available through the `Stilism` tool[3] (Capitanio et al. 2017; Lallement et al. 2018), the reddening towards our target is negligible. Thus we assumed $E(B-V)=0$ in our fitting. By adopting solar metallicity and a $\log g$ of 4.5 dex, our χ^2 minimization yielded an effective temperature of 3900±70 K for CP−72 2713. Using the inferred photosphere model and the Gaia DR2 distance of the object we derived a luminosity of 0.18±0.01 $L_\odot$ and a stellar radius of 0.94±0.04 $R_\odot$. To estimate the stellar mass and age, the effective temperature and the obtained luminosity values were compared to the theoretical predictions of the MESA Isochrones and Stellar Tracks (MIST, Choi et al. 2016; Dotter 2016). In the course of isochrone fitting we followed the method described by Pascucci et al. (2016), that yielded $0.71^{+0.03}_{-0.05}$ $M_\odot$ and 14^{+5}_{-3} Myr for the best-fit mass and age, respectively. Considering the uncertainties, the estimated age is satisfactorily consistent with that of the BPMG (24±3 Myr, Bell et al. 2015). We note that the derived stellar mass and radius results in a $\log g$ of 4.34 dex, adequately confirming our a priori assumption. The stellar parameters are summarized in Table 3.

3.2. *Stellar activity*

Similarly to other young late-type stars, CP−72 2713 shows strong stellar activity that manifests in various indicators. It has an X-ray counterpart in the ROSAT catalog implying a fractional X-ray luminosity of $\log L_X/L_{bol} = -2.92$ (Kiraga 2012). This is close to the saturation value of -3, indicating strong coronal activity. The star was also detected by the GALEX satellite (Martin et al. 2005) both in the near- (NUV) and far-UV (FUV) bands. By combining these photometric data with 2MASS measurements and placing the object in the $NUV-J$ vs. $J-K$ color-color diagram, compiled by Findeisen et al. (2011), we found that its position matches well the locus of other BPMG members. This implies significant excess at UV wavelengths, which is likely due to prominent chromospheric activity.

CP−72 2713 has already been observed by The Transiting Exoplanet Survey Satellite (*TESS*, Ricker et al. 2015) providing a very precise, ∼52 days long photometric data set with a cadence of 2 minutes. Reduction and analysis of these *TESS* data are described in details in Appendix A. As further signatures of activity, CP−72 2713 exhibits flares and rotational modulation due to stellar spots in its *TESS* light curve (Fig. 7). Consistently with previous ASAS based results of 4.456 days (Kiraga 2012) and 4.48 days (Messina et al. 2010) we obtained a rotation period of P = 4.437 d from a Fourier analysis of our light curve. In addition, we identified 51 flares or group of flares. We found that the star spent about 936 minutes in flaring state, which is 1.24% of the time covered by *TESS*.

[3] https://stilism.obspm.fr/

Table 3. Stellar parameters

Parameter	Data	References
Distance (pc)	36.62±0.03 pc	Bailer-Jones et al. (2018)
Spectral type	K7Ve	Torres et al. (2006)
	K7IVe	Pecaut & Mamajek (2013)
	M0	Gaidos et al. (2014)
$T_{\rm eff}$ (K)	3900±70 K	This work
L_* ($L_\odot$)	0.18±0.01	This work
R_* ($R_\odot$)	0.94±0.04	This work
M_* ($M_\odot$)	$0.71^{+0.03}_{-0.05}$	This work
L_X/L_{bol}	-2.92	Kiraga (2012)
$v \sin i_*$ (kms^{-1})	7.1±0.9[a]	Torres et al. (2006)
		Weise et al. (2010)
$P_{\rm rot}$ (days)	4.437	This work
$v_{\rm rad}$ (kms^{-1})	8.0±0.4[a]	Torres et al. (2006)
		Lindegren et al. (2018)

[a] Weighted average of the values reported by the cited papers.

3.3. *Disk properties*

To construct the spectral energy distribution (SED) of our target at $\lambda > 5\mu$m, the already reported *Spitzer*, *Herschel* and ALMA data were supplemented by additional spaceborne mid-infrared photometry obtained by the *AKARI* and *WISE* satellites. The SED was further supplemented by a recent observation obtained with the ATCA at 9 mm (Brodie et al. in prep.). The available photometric data, as well as the predicted photospheric flux densities in the specific bands are given in Table 1. The uncertainty of the predicted photospheric fluxes is estimated to be 5%. The compiled SED together with the photosphere model are displayed in Figure 2. While at wavelengths shortward of 25μm the measured flux densities are consistent with the predicted photospheric contribution, in the far-IR and millimeter regime CP−72 2713 exhibits significant excess emission that arises from an extended circumstellar dust disk (Sect. 2). To estimate the characteristic temperature ($T_{\rm d}$) and fractional luminosity ($f_{\rm d} = L_{\rm disk}/L_{\rm bol}$) of this disk, we fitted the excess emission by a single temperature modified blackbody model where the emissivity is 1 at wavelengths shorter than λ_0 and varies as $(\lambda/\lambda_0)^{-\beta}$ at longer wavelengths. This model accounts for the general observational results that the emission of debris disks exhibits a fall at wavelengths that are large

relative to the typical size of the emitting grains. Because of the sparse wavelength coverage, the λ_0 parameter could not be adequately constrained in our case, thus in the fitting we fixed its value to 100μm. We adopted a Levenberg-Marquardt approach (Markwardt 2009) in searching for the best-fitting model. During the fitting process we used an iterative way to compute and apply color corrections for our photometric data. As a result we derived a dust temperature of 43±3 K and a β of 0.05±0.08. The low β value indicates an excess spectrum that is almost identical to a pure blackbody and therefore changing the λ_0 parameter has no effect on our results. We note that though most debris disks show considerably steeper millimeter slopes (Gáspár et al. 2012; MacGregor et al. 2016; Marshall et al. 2017), interestingly, the excess SED of AU Mic can also be well reproduced by a blackbody (Matthews et al. 2015). For the fractional luminosity we obtained $f_{\rm d} = 1.1 \times 10^{-3}$.

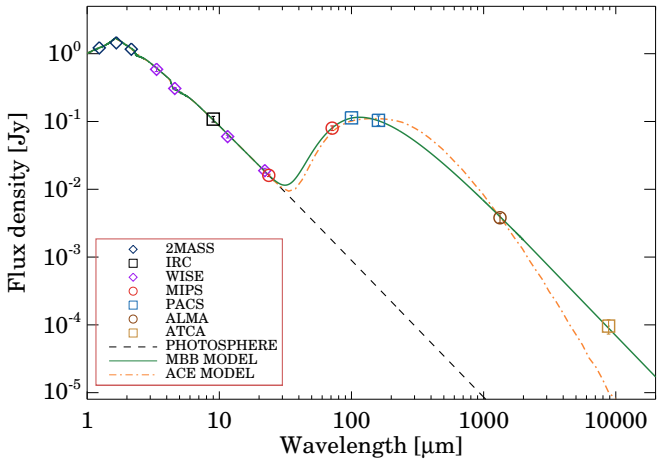

Figure 2. Color-corrected SED of CP−72 2713. The green curve shows the best fitting modified blackbody model. As a comparison, the orange curve shows an Analysis of Collisional Evolution (ACE) model for the disk with a total mass of 50 $M_\oplus$ was also overplotted (see Sect. 4.3). This shows the model SED after 24 Myr of evolution assuming $\dot{M}_{*,\rm wind} = 300\dot{M}_{\odot,\rm wind}$.

3.3.1. *The dust component*

Using our ALMA millimeter measurement we estimated the dust mass in grains of sizes smaller than a few millimeter ($M_{\rm d}$). Assuming optically thin dust emission that can be characterized by a single dust temperature, the dust mass

$$M_d = \frac{F_\nu d^2}{B_\nu(T_{\rm dust})\kappa_\nu}, \qquad (1)$$

where d is the distance, $B_\nu(T_{\rm dust})$ is the Planck function at 1.33 mm for the characteristic dust temperature, and κ_ν is the dust opacity at the given frequency. Dust particles with size >100μm, whose radiation dominates the emission at this wavelength (Hughes et al. 2018), are thought to behave like blackbodies. At a radial distance of 140 au from CP−72 2713, a star with a luminosity of 0.18 $L_\odot$ (Sect. 3.1), the temperature of such grains is ∼15 K. By adopting κ_ν =2.3 cm^2 g^{-1} for the dust opacity (Andrews et al. 2013), Eq. 1 provides a dust mass estimate of 0.21±0.03 $M_\oplus$. The quoted uncertainty accounts for the errors of the measured flux density and the distance of the system. Note, however, that the potential systematic uncertainties of the dust opacity can introduce even a factor of 2–3 difference in the estimate (e.g. Miyake & Nakagawa 1993; Ossenkopf & Henning 1994) and the dust temperature may not be characterized by a single value. These factors were not considered in our error calculations.

3.3.2. *The gas component*

To derive an upper limit for the total CO gas mass using the measured ^{12}CO integrated line flux upper limit, we need to estimate the fraction of CO molecules that populate the upper level of the 2–1 rotational transition. Collisions of CO molecules with different gas constituents, radiative processes, and UV pumping (Matrà et al. 2015, 2019) can all affect the population of the rotational levels. Based on the available data, it is difficult to judge the relative importance of these processes in the excitation. In our calculations we assumed that local thermodynamic equilibrium holds, i.e. that collisions dominate the excitation processes and that gas emission is optically thin. Adopting gas temperatures between 10 and 45 K we derived CO mass upper limits in the range of 6.8–9.4×10^{-6} $M_\oplus$.

3.4. *Source confusion and contamination check*

So far in our analysis we have assumed that the observed excess emission solely originates from a circumstellar disk. Knowing the main properties of the source, at this point it is worth assessing the possibility of source confusion as well as potential influence of different kind of contaminations.

First we examine whether the excess could come from a background galaxy. Based on the recently derived double power-law model of the cumulative number counts of galaxies at millimeter wavelengths (González-López et al. 2020) we estimated a probability of ∼0.006 of the presence of a background galaxy brighter than 3.8 mJy within the primary beam of the ALMA 7-m array. If we consider only the interferometric synthesized beam, this value is reduced to ∼1.1×10^{-4}.

Besides the low probability of positional coincidence, there are other strong arguments against this scenario. We measured an angular size of $\sim 7\farcs5$ for the emitting structure at 1.3 mm. As interferometric observations show, galaxies are compact at (sub)millimetric wavelengths with a typical size of $0\farcs3 \pm 0\farcs1$ (Franco et al. 2018, and references therein), i.e., they are significantly smaller than our source. The SED of the measured excess emission towards CP−72 2713 peaks at $\sim 120\mu$m and has a millimeter spectral index of ~ 2. Although the SEDs of local (low-redshift) galaxies peak at a similar wavelength, their millimeter spectral slope is significantly steeper with typical indices between 3.5 and 4.0 (Casey et al. 2014). Moreover, such low-redshift objects represent only a small fraction of known millimeter galaxies (Casey et al. 2014, and references therein).

Lensed galaxies deserve a special attention since gravitational lensing effect can magnify distant background sources thereby increasing both their fluxes and angular sizes. At the spatial resolution we achieved in our ALMA observation, multiple images of lensed galaxies can mimic a source having more comparable size to that of our target than normal (unlensed) dusty galaxies. However, despite their significant contribution to the bright-end population of galaxies at submm/mm wavelengths, lensed dusty star-forming galaxies are rare objects with a sky density of 0.1–0.2 deg^{-2} (Casey et al. 2014; Negrello et al. 2010, 2017; Wardlow et al. 2013). Thus the probability that such an object appears within the primary beam of our millimeter observation is less than 4×10^{-5}. The shape of their SEDs also deviates from what we measured towards CP−72 2713: the redshifts of lensed galaxies are typically >2 (Vieira et al. 2013), their long wavelength emission peaks at $\gtrsim 250\mu$m (Negrello et al. 2017).

Although it is very unlikely that all observed excess is coming from a background galaxy, owing to our coarse spatial resolution, positional coincidence with fainter extragalactic objects cannot be completely ruled out. Recent high spatial resolution millimeter images of several debris disks show compact sources – most likely background galaxies – co-located or located close to the dust ring (Chavez-Dagostino et al. 2016; Booth et al. 2017; Marino et al. 2017; Su et al. 2017; Faramaz et al. 2019). Such objects, if present, can contribute to the measured emission at far-IR and millimeter wavelengths and can modify the derived millimeter spectral index of our target. Higher resolution millimeter observations are needed to explore these possible contaminating sources and to assess their role, e.g., in the observed unusually shallow millimeter slope.

In our analysis the modelling of the stellar contribution to the measured emission was limited to the photospheric fluxes. However, at millimeter wavelengths low mass active stars can exhibit non-photospheric emission (e.g., Liseau et al. 2015; MacGregor et al. 2015). Recent millimeter ALMA observations of AU Mic revealed a central point source at the star's position with a flux density $\sim 6\times$ higher than predicted based on the pure photospheric model (MacGregor et al. 2013). The observed excess was attributed either to an inner dust belt (MacGregor et al. 2013) or coronal emission from the star itself (Cranmer et al. 2013). In the case of CP−72 2713 the 1σ measurement uncertainty (0.37 mJy) of the 1.33 mm observation is $\sim 80\times$ higher than the predicted photospheric flux density. Supposing that the non-photospheric contribution at CP−72 2713 is not stronger than in the case of AU Mic (based on their fractional X-ray luminosity, see Kiraga 2012, the coronal activity levels of the two stars are similar) i.e. $\lesssim 6\times$ the photospheric emission, the measurement uncertainty is significantly higher than the uncertainty of the stellar flux prediction. For shorter periods, however, a higher level of activity cannot be excluded. As it was demonstrated in the cases of Proxima Cen and AU Mic, a strong flare can enhance a star's millimeter flux by orders of magnitudes for a few tens seconds (MacGregor et al. 2018; Daley et al. 2019). White et al. (2018) also found significant variability in the 9 mm emission of the young M-type star, HD 141569 B, throughout its $\sim$1 hr observation. By examining the obtained ALMA data stream of CP−72 2713, we found no evidence for such flux enhancements. Actually, this meets our expectations: we identified only 51 flare events in the 52 days long TESS light curves (Sect. 3.2), and found that the star spends only $\sim$1.2% of time in flare phase in the studied period (in fact the peaks of the flares, which can substantially contribute to the millimeter emission, covers even much less time). Based on all of this, we believe that most of the measured millimeter flux is due to the dust disk.

3.5. *Star-disk alignment*

For the projected rotational velocity of the star, Torres et al. (2006) obtained a value of $v \sin i_* = 7.5 \pm 1.2$ km s^{-1}, while Weise et al. (2010) quoted $v \sin i_* = 6.6 \pm 1.4$ km s^{-1} in their work. Computing the weighted mean of these $v \sin i_*$ measurements and using the rotational period (in days) and the stellar radius derived above (in solar radii), following Campbell & Garrison (1985) and Greaves et al. (2014) we estimated the inclination of the stellar pole with

respect to the line of sight as:

$$\sin i_* = 0.0198 \frac{Pv \sin i_*}{R_*}. \quad (2)$$

This yields an inclination of $i_* = 42 \pm 7°$, that is in good agreement with the disk inclination obtained from the analysis of our ALMA data (Sect. 2.3). This finding coincides well with the conclusions made by Watson et al. (2011), Kennedy et al. (2013) and Greaves et al. (2014): by examining larger debris disk samples these authors also found no evidence for significant misalignment between the stellar equator and the disk in the studied systems.

4. DISCUSSION

4.1. *Evolutionary status of the disk*

A noteworthy fraction of members in ∼24 Myr old BPMG exhibit excess emission at infrared wavelengths (Rebull et al. 2008; Riviere-Marichalar et al. 2014; Moór et al. 2016). While in most of these systems the observed excess is likely attributed to thermal emission of tenuous circumstellar debris disks, at least one member of this group, the late-type close binary V4046 Sgr harbors a long-lived gas-rich protoplanetary disk (e.g. Rosenfeld et al. 2013). Thus, the presence of a protoplanetary disk even at the age of BPMG is not unseen. Therefore in the following we will examine the nature of CP−72 2713 disk.

Observationally one of the most conspicuous differences between protoplanetary and debris disks is related to the amount of dust. While protoplanetary disks with their larger dust content are optically thick at most wavelengths, debris disks are optically thin across the spectrum. This is manifested in the fractional luminosities, the threshold between the two classes is typically set to $f_d = 0.01$, which is about 10× higher than that of CP−72 2713. The estimated dust mass of ∼0.2 $M_\oplus$ in our target matches well those of other debris disks (Holland et al. 2017). Recent large surveys of protoplanetary disks implied a positive correlation between disk radius and millimeter continuum luminosity (e.g. Andrews et al. 2010; Tripathi et al. 2017; Hendler et al. 2020). The relationship between the effective disk radii ($R_{\rm eff}$) and the millimeter continuum luminosity ($L_{\rm mm}$) was studied in five nearby star forming regions (Ophiuchus, Taurus-Auriga, Chameleon I, Lupus, Upper Sco) by Hendler et al. (2020). In their work $R_{\rm eff}$ was defined as the radius that encircles 68% of the continuum emission, while $L_{\rm mm}$ was the Band 7 flux density scaled to 140 pc. Using our SED model (Sect. 3.3) we estimated a flux density of 8.4 mJy at 890μm for CP−72 2713, that results in $L_{\rm mm} \sim 6 \times 10^{-4}$ Jy. With its low luminosity and large size of the disk, CP−72 2713 deviates significantly from the observed relationships: protoplanetary disks with $R_{\rm eff} > 100$ au have at least two orders of magnitudes higher $L_{\rm mm}$. The dust properties of our target seem inconsistent with a protoplanetary nature.

The mass of protoplanetary disks is dominated by their gas component, which is no longer present in significant quantities in most debris disks (Wyatt et al. 2015; Kral et al. 2018). We observed no CO emission towards CP−72 2713. The obtained 3σ upper limit on the ^{12}CO (2–1) line luminosity is about three orders of magnitude lower than that of the protoplanetary disk around V4046 Sgr (Rosenfeld et al. 2013). We note that ^{12}CO in V4046 Sgr is optically thick, suggesting an even higher contrast in the gas mass ratio between the two systems. Even more indicatively this upper limit also remains six times below the measured ^{12}CO (2–1) line luminosity of the disk of β Pic, whose gas and dust components are attributed to collisional erosion of larger bodies thus found to be of second generation (Kral et al. 2016; Matrà et al. 2017b; Cataldi et al. 2018). Torres et al. (2006) and Gaidos et al. (2014) found the Hα line in emission in CP−72 2713 with measured equivalent widths of 1.9 Å and 0.84 Å, respectively. Based on the criteria proposed by Barrado y Navascués, & Martín (2003) these values can be explained with chromospheric activity and do not indicate ongoing accretion and thus the presence of an inner gas-rich disk.

These findings suggest that our target harbors a gas poor disk and, together with the results on the dust component, favors the classification of CP−72 2713 as a debris disk.

Nevertheless, with its fractional luminosity of 1.1×10^{-3} this disk is considered as a very dust-rich system among debris disks. By comparing this value with that of other cold debris disks with late-type host stars in the BPMG, we can find that it is about 3× higher than that of the iconic disk of AU Mic (3.5×10^{-4}, Matthews et al. 2015) and matches well the fractional luminosity of the debris disk around AG Tri (10^{-3}, Riviere-Marichalar et al. 2014). Beside CP−72 2713 we know only four debris systems within 40 pc of the Sun that have well established cold dust component and exhibit fractional luminosity higher than 10^{-3}, namely β Pic, HD 61005, TWA 7 and HD 107146.

Despite its large dust content and proximity, the disk of CP−72 2713 has remained undiscovered for a long time. This is largely due to the low luminosity of the host star: the system does not exhibit excess at mid-infrared wavelengths observed by the *WISE* satellite and its far-infrared emission falls below the detection limit

of all-sky surveys performed by the *IRAS* and *AKARI* satellites.

4.2. *Dust removal mechanisms*

In steady state, the production of dust particles by collisions in debris disks is balanced by grain removal processes through radiation and stellar wind forces. In most known debris disks around main-sequence stars, the stellar radiation pressure plays an important role in controlling the dust dynamics by driving particles on more eccentric orbits than those of their parent bodies, and by expelling grains small enough from the system (e.g. Krivov 2010). In lower luminosity K- and M-type stars, however, the radiation pressure is not strong enough to remove grains (Plavchan et al. 2005; Reidemeister et al. 2011; Schüppler et al. 2015).

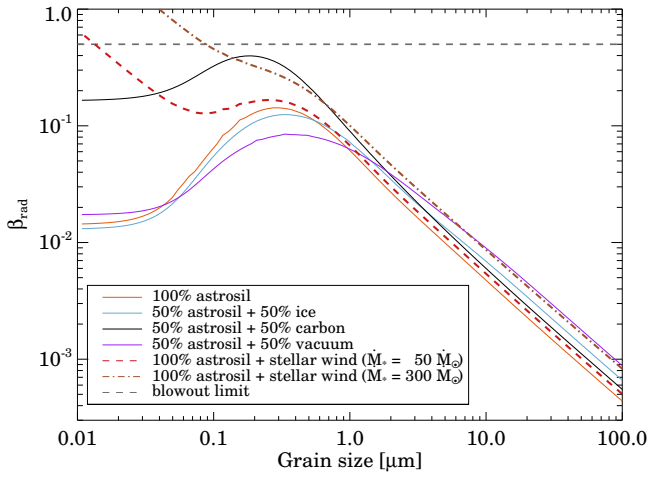

Figure 3. The $\beta_{\rm rad}$ ratio as a function of grain size for different dust compositions. Influence of the stellar wind pressure force is also explored for two different wind mass loss rates. Blowout limit of β=0.5 is marked by a dashed horizontal line.

Figure 3 shows the ratio of radiation to gravitational force, $\beta_{\rm rad} = \frac{F_{\rm rad}}{F_{\rm grav}} = \frac{3L_*Q_{\rm pr}}{16\pi GM_*c\rho s}$ (Burns et al. 1979), for compact spherical dust grains with different ρ densities and s sizes in the CP−72 2713 system. We explored four different grain compositions, for which the $Q_{\rm pr}$ radiation pressure efficiency was computed by means of Mie theory using the code developed by Bohren & Huffman (1983). Assuming parent bodies on a circular orbit the released grains become unbound if their $\beta_{\rm rad}$ is >0.5. As Fig. 3 demonstrates, $\beta_{\rm rad}$ remains below this critical value for each tested dust composition, i.e. none of the particles are expelled by the radiation pressure in the CP−72 2713 system. We note that as an active star, CP−72 2713 exhibits excess at UV wavelengths, shows strong coronal X-ray emission (Sect. 3.2), and during flares its short wavelength emissions increases further. Our stellar model does not account for these effects and thus we likely underestimate the strength of the radiation pressure. In the case of AU Mic whose UV, EUV, and X-ray emission is better constrained by observations than that of our target, Augereau & Beust (2006) found that this excess radiation is most important in flare state when the $\beta_{\rm rad}$ value could be even a few times higher.

The stellar wind mass loss of magnetically active late-type stars, as CP−72 2713 (Sect. 3.2), is thought to significantly exceed the solar value (e.g. Wargelin & Drake 2001; Wood et al. 2002). In such systems wind forces can dominate the dust removal (Plavchan et al. 2005; Strubbe & Chiang 2006; Augereau & Beust 2006). Considering this corpuscular component as well, the ratio of the radiation and wind forces to gravitational force can be calculated following Strubbe & Chiang (2006):

$$\beta_{\rm rad} = \frac{F_{\rm rad} + F_{\rm sw}}{F_{\rm grav}} = \frac{3L_*P_{\rm swr}}{16\pi GM_*c\rho s}, \qquad (3)$$

where $P_{\rm swr} \equiv Q_{\rm pr} + Q_{\rm sw}\frac{\dot{M}_{*,\rm wind}v_{\rm wind}c}{L_*}$. In this formula $Q_{\rm sw}$ is the stellar wind coupling coefficient, that gives the ratio of the effective to geometric cross section, $\dot{M}_{*,\rm wind}$ is the stellar wind mass loss rate, while $v_{\rm wind}$ is the stellar wind velocity. No data is available on the wind mass loss rate of our target in the literature. For the similarly active AU Mic, Augereau & Beust (2006) derived mass loss rates of 50 and 300× higher than that of our Sun ($\dot{M}_{\odot,\rm wind} = 2\times10^{-14}M_\odot{\rm yr}^{-1}$) by taking its quiescent phase and considering the influence of episodic flare activity, respectively. Using these mass loss rates and adopting $Q_{\rm sw} = 1$ and a wind velocity of 400 km s^{-1} (that corresponds to the average wind velocity of the Sun) we recomputed the β values for astrosilicate particles. As Figure 3 shows, particles with sizes smaller than ∼0.013μm in the $\dot{M}_{*,\rm wind} = 50\dot{M}_{\odot,\rm wind}$ scenario and ∼0.09μm in the $\dot{M}_{*,\rm wind} = 300\dot{M}_{\odot,\rm wind}$ scenario have a β value >0.5. Thus by considering the possible wind pressure these small grains are blown out from the system.

The Poynting-Robertson (P-R) drag as well as the stellar wind drag also affect the dynamics of dust particles: producing effective forces opposite to the direction of the orbital motion, these drags result in a gradual lose of the grains' angular momentum and lead them to spiral into the star. Assuming a particle originally having a circular orbit, the time necessary to reach the central star from a radius R under the effect of P-R drag can be computed as $t_{\rm P-R}({\rm yr}) = 400\frac{R({\rm au})^2}{M_*(M_\odot)}\frac{1}{\beta_{\rm rad}}$ (Wyatt 2005). Taking the disk radius of 140 au (Sect. 2.3), during the lifetime of the system (∼24 Myr) only grains

with $\beta_{\rm rad} > 0.45$ could have spiraled into the star. Since the collision cascade probably started well after the birth of the system (see Sect. 4.6), then the available time is even shorter and the threshold value for β is even larger. The stellar wind drag can work on a shorter timescale. According to Plavchan et al. (2005) $\frac{t_{\rm P-R}}{t_{\rm sw}} = \frac{Q_{\rm P-R}}{Q_{\rm sw}} \frac{\dot{M}_{*,\rm wind} c^2}{L_*}$, thus by assuming $\frac{Q_{\rm P-R}}{Q_{\rm sw}} = 1$ and using the adopted $\dot{M}_{*,\rm wind}$ values of $50\dot{M}_{\odot,\rm wind}$ or $300\dot{M}_{\odot,\rm wind}$ the timescale of the wind drag could be ∼80 or ∼480 shorter, than the P-R timescale and can result in significant inward transport of larger dust particles as well. In the following we will investigate how these effects, considering the influence of collisions, can affect the spatial distribution of grains.

4.3. *Collisional evolution*

We utilized the Analysis of Collisional Evolution (ACE, Krivov et al. 2006; Löhne et al. 2008) modelling code that can simulate the collisional evolution of the disk as well as the impact of transport processes on the dust distribution. By solving numerically the Boltzmann-Smoluchowski kinetic equation this code enables to follow the evolution of a disk composed of subplanetary sized bodies down to micron-sized dust particles, considering the outcomes of collisions between these solids as well as the influence of stellar gravity force and stellar radiative/corpuscular forces on them. ACE has already been applied successfully to explore the long term evolution of several debris disks (e.g. Löhne et al. 2012; Reidemeister et al. 2011; Schüppler et al. 2015; Geiler et al. 2019).

In our simulations we used the stellar and disk parameters derived in this work. We adopted a stellar mass of 0.71 $M_\odot$ and a luminosity of 0.18 $M_\odot$, while for the stellar SED we used the ATLAS9 atmosphere model compiled in Sect. 3. Based on the best fit model of the millimeter emission (Sect. 2.3) the parent planetesimal belt was assumed to be located between 126 and 154 au corresponding to a radial extent of $0.2R$, with $R = 140$ au. We set a uniform surface density for this ring. For the initial mass distribution of the solids we assumed a power-law with an index of -1.88 (Gáspár et al. 2012; Krivov et al. 2018). The largest planetesimals were 10^{21}g (∼40km in radius; note that this size is not constrained, but was chosen to be sufficiently high to give a threshold for the collisional cascade), while the smallest particles were 10^{-13}g (sub-micron sized). The average initial orbital eccentricity of the planetesimals was set to 0.03. Regarding the setup of the critical specific energy for disruption we followed that described by Löhne et al. (2012). To explore the influence of the stellar wind we performed simulations with three different wind mass loss rates of $\dot{M}_{*,\rm wind} = 0$, $50\,\dot{M}_{\odot,\rm wind}$, and $300\,\dot{M}_{\odot,\rm wind}$. The wind velocity was set to 400 km s^{-1} in all three models. We followed the disk evolution for 24 Myr. By assuming pure astronomical silicate (Draine 2003) as dust material, we calculated the SED of the simulated disks (for details see Pawellek et al. 2019). We found that disk models with a mass of 50 $M_\oplus$ – which include all solids up to the maximum size of 40 km – reproduce the measured SED at wavelengths ≤ 1.3 mm well, although they cannot account for the unusually shallow millimeter SED, and thus substantially underestimate the observed flux at 9 mm (see Figure 2 for an example). It is yet unclear what may be the reason for the measured low millimeter spectral index, but several different factors, including external contaminations (e.g. by galaxies, see Sect. 3.4), may play a role. To clarify these, and refine the model further, higher spatial resolution images are needed.

Using the 50 $M_\oplus$ models we generated thermal maps at 100μm and 1.3 mm. Figure 4 displays normalized surface brightness profiles as a function of radial distance at these two wavelengths after 1, 10 and 24 Myr evolution of the disk. These profiles were compiled as the azimuthal average of the thermal maps. Assuming that the stellar wind is negligible (Fig. 4a), we do not see significant differences between disks with different evolutionary states. This is consistent with the results of the above analytical calculations (Sect. 4.2): the stellar radiation force itself is too weak to substantially modify grains' orbit. However, in models with stellar wind, the inward migration of dust particles becomes efficient due to the wind drag (Fig. 4bc). At 1.3 mm this has no significant impact on the surface brightness distribution. The thermal emission peaks at the planetesimal belt, the inner regions are two orders of magnitude fainter even in the $\dot{M}_{*,\rm wind} = 300\,\dot{M}_{\odot,\rm wind}$ model. This finding is consistent with the results obtained by Pawellek et al. (2019) for debris disks around late-type stars with stellar wind. At 100μm, where smaller grains dominate the emission, the influence of the wind drag is more visible: though the birth ring is still the brightest part of the disk, especially in the model with the strongest wind the surface brightness inside the ring is only a few times lower.

4.4. *Possible signature of stellar wind drag?*

Interestingly, by analyzing the PACS image we obtained a smaller disk radius (99^{+22}_{-26} au) than from the ALMA data (140±14 au). Though taking into account the uncertainties the difference between the two estimated radii is formally not significant, in the light of the ACE results it is worth examining whether it could

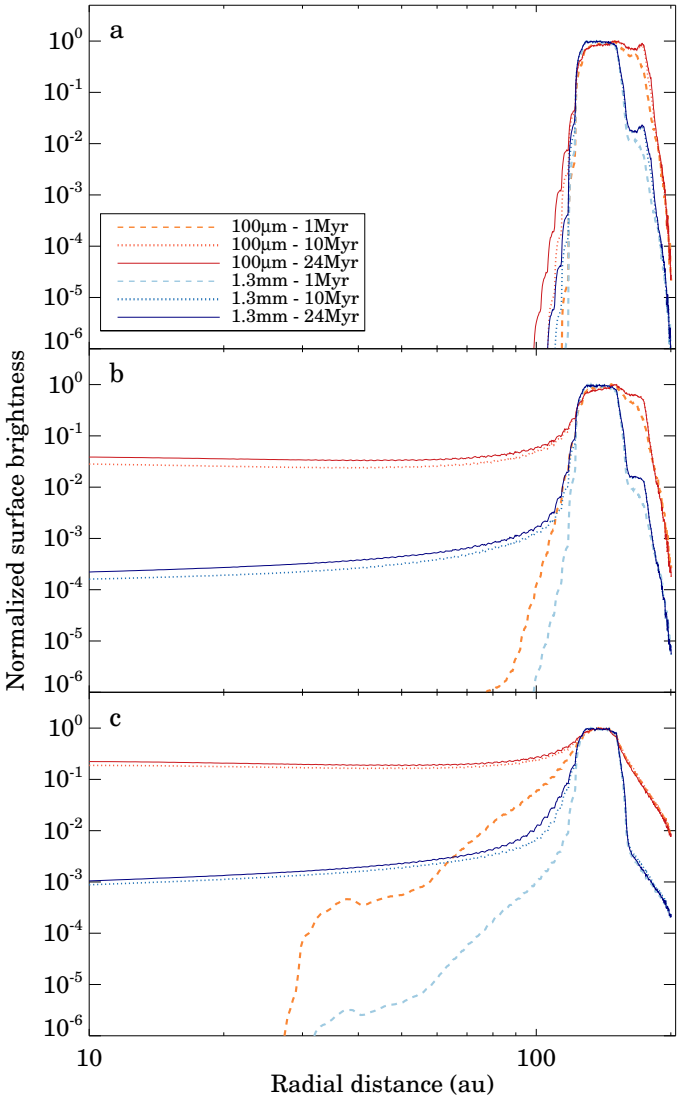

Figure 4. Normalized surface brightness at 100μm and at 1.3 mm as a function of radial distance at three different evolution time. From top to bottom, adopting different stellar wind mass loss rates of (a) $\dot{M}_{*,\mathrm{wind}} = 0$, (b) $\dot{M}_{*,\mathrm{wind}} = 50\dot{M}_{\odot,\mathrm{wind}}$, and (c) $\dot{M}_{*,\mathrm{wind}} = 300\,\dot{M}_{\odot,\mathrm{wind}}$.

be the effect of wind drag. We constructed simulated PACS images from the 100μm thermal model maps by convolving them with our PSF model (Sect. 2.2). Then, using these simulated data we derived the disk peak radius by fitting the same Gaussian ring model as we applied in the case of the real data (Sect. 2.2). For most simulations the derived peak radii were around 140 au, i.e. the surface brightness distribution is dominated by the parent belt. However, for the most extreme model with $\dot{M}_{*,\mathrm{wind}} = 300\,\dot{M}_{\odot,\mathrm{wind}}$ at 24 Myr we obtained a peak radius of 114 au.

This result indicates that if the stellar wind is strong enough, then it may be able to shape the spatial distribution of grains so that the belt appears smaller at 100μm. We note, however, that taking into account that the formation of planetesimals and then the proper stirring of the disk (see Sect. 4.6) needs time, the evolutionary time is likely substantially shorter than 24 Myr. Thus, if the differences between the 100μm and 1.3 mm measurements are real and related to transport processes then this simulation suggests a $\dot{M}_{*,\mathrm{wind}} > 300\,\dot{M}_{\odot,\mathrm{wind}}$ for this system.

Thanks to its large angular size and advantageous orientation the disk around CP−72 2713 could be an ideal target to investigate the influence of wind dominated transport in the future, however it needs high resolution multiwavelength observations that allow the study of radial profile of the emitting regions.

4.5. *Location of the planetesimal belt*

Up to now about two dozens of debris disks have been spatially resolved at (sub)millimeter wavelengths, allowing to constrain the location of the outer planetesimal belts in these systems. Using these data, Matrà et al. (2018) found a relationship between stellar luminosity L_* and disk radius in the form of $R(\mathrm{au}) = 73^{+6}_{-6} L_*(L_\odot)^{0.19^{+0.04}_{-0.04}}$. This formula predicts a disk radius of 53±6 au for CP−72 2713, which is significantly smaller than the measured size of 140 au. To further explore this aspect, in Fig. 5 we displayed the outer radii[4] of six debris disks (ϵ Eri, AU Mic, HD 61005, TWA 7, HD 92945, and HD 107146) hosted by stars with masses between 0.5 and 1.0 $M_\odot$ (similar to that of CP−72 2713) as a function of age. We have selected only objects that are younger than 1 Gyr and whose estimated radii are based on spatially resolved millimeter observations (Booth et al. 2017; Daley et al. 2019; MacGregor et al. 2018; Matrà et al. 2019; Marino et al. 2018, 2019) and thus thought to represent the outer edge of their planetesimal belts. Age estimates of these systems are taken from the literature (Mamajek & Hillenbrand 2008; Bell et al. 2015; Zuckerman 2019; Marino et al. 2019; Williams et al. 2004). Similarly to CP−72 2713, these objects represent the most dust-rich known debris disks hosted by late-type stars in our neighbourhood. As Fig. 5 demonstrates, the disk radius of our target is comparable to those of HD 92945 and HD 107146, and is substantially larger than those of the other three debris systems.

[4] In the case of HD 61005, MacGregor et al. (2018) modelled the observed millimeter data using a two-component model composed by a planetesimal belt and an outwardly extended halo. In our study we used the outer radius of the planetesimal belt component (67 au).

This is especially remarkable when considering that in the case of CP−72 2713 we displayed the estimated peak radius of the belt instead of the outer radius (because of the limited angular resolution, the disk width was fixed in our modelling). Thus, CP−72 2713 is not just very dust-rich, but it is unusually extended.

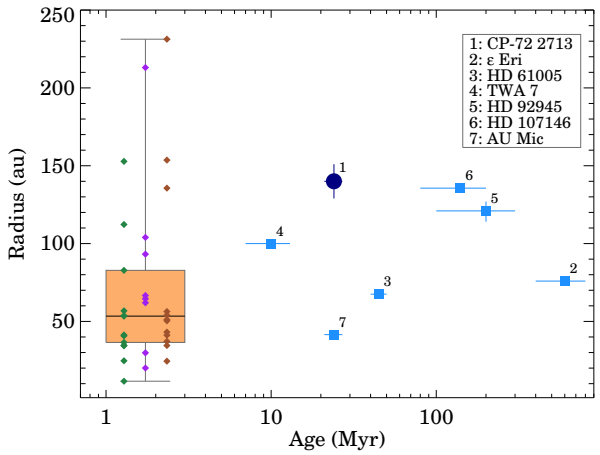

Figure 5. Disk outer radius as a function of age. For CP−72 2713 the best-fit peak disk radius is displayed by a large dark blue circle. Blue squares denote debris disks. Protoplanetary disks belonging to the Taurus, Lupus, and Chamaeleon I star forming regions are marked by green, purple, and brown diamonds, respectively. The position of the points does not represent ages but serves to better distinguish the stars belonging to different regions. The shaded region represents the 25–75% quartiles of the disk size distribution. The whiskers correspond to the 0–25% and 75–100% quartiles.

Assuming that the planetesimal belt in the CP−72 2713 system is still close to its birthplace, we can expect that the predecessor protoplanetary disk must have contained a concentration of a large amount of material at the same radius. Thus it is interesting to compare the size of our disk with the measured outer radii of protoplanetary disks around similar mass (0.5–1.0 $M_\odot$) young stars. Thanks to recent ALMA observations, there is a growing sample of protoplanetary disks resolved at millimeter wavelengths in the continuum. In Figure 5 we plotted the outer radii of 33 such protoplanetary disks belonging to the Lupus, Chamaeleon I, and Taurus star forming regions. The ages of these groups range between 1 and 3 Myr. The disk size estimates of Lupus and Chamaeleon I objects were taken from Hendler et al. (2020). We used their R_{90} radii that are defined as radius containing 90% of the millimeter continuum flux. For disks in Taurus we used the data from Long et al. (2018) and Long et al. (2019), who derived R_{90} and R_{95} radii, respectively. In Figure 5, the shaded orange box shows the 25–75% quartiles of the size distribution, while the whiskers represent the 0–25% and 75–100% quartiles. The median disk radius is denoted by a horizontal black line. We note that due to observational biases towards brighter objects the plotted disks likely represent the most massive/extended category of protoplanetary disks. Figure 5 shows that CP−72 2713 is not only the most extended debris disk but its radius is comparable to the largest protoplanetary disks in the studied stellar mass range.

4.6. *Stirring of the planetesimal belt*

After the dispersal of the gas-rich protoplanetary disks the leftover planetesimals are thought to have nearly circular orbits, likely resulting in non-destructive, low velocity collisions between them. To ignite an effective collisional cascade, that produces a continuous replenishment of dust particles observable at infrared and millimeter wavelengths, the planetesimal disk needs to be dynamically excited. The possible reasons of this dynamical excitation are still debated in the literature. The most commonly invoked explanations require the existence of a giant planet or a stellar companion somewhere in the system (planetary or binary stirring, Mustill & Wyatt 2009) or/and the presence of large planetesimals embedded in the belt (self-stirring, Kenyon & Bromley 2008). In our Solar System both self-stirring and planetary stirring may contribute to the excitation of the Kuiper-belt, resulting in a high excitation level there (Matthews et al. 2014). However, our knowledge is limited on the origin of stirring in other debris disks (Moór et al. 2015; Krivov & Booth 2018). All proposed stirring mechanisms need time to be activated in a given part of the disk. Using the model predictions thus we can examine their feasibility in the CP−72 2713 system.

According to the classical version of the self-stirring model (Kenyon & Bromley 2008), mutual low velocity collisions between smaller bodies in a dynamically cold region of the disk lead to the formation of gradually larger planetesimals. Kenyon & Bromley (2008) found in their simulations that after reaching a radius of ∼1000 km the largest planetesimals can stir their environment efficiently. It makes collisions between their smaller neighbours destructive and leads to the production of debris material through a collisional cascade. Adopting an initial protoplanetary disk with a surface density distribution of $\Sigma(a) = 0.18(M_*/M_\odot)x_{\rm m}(r/30{\rm au})^{-3/2}{\rm g\ cm^{-2}}$, where $x_{\rm m}$ is a scaling factor (for the minimum-mass solar nebula $x_{\rm m} \equiv 1$), Kenyon & Bromley (2008) provided an an-

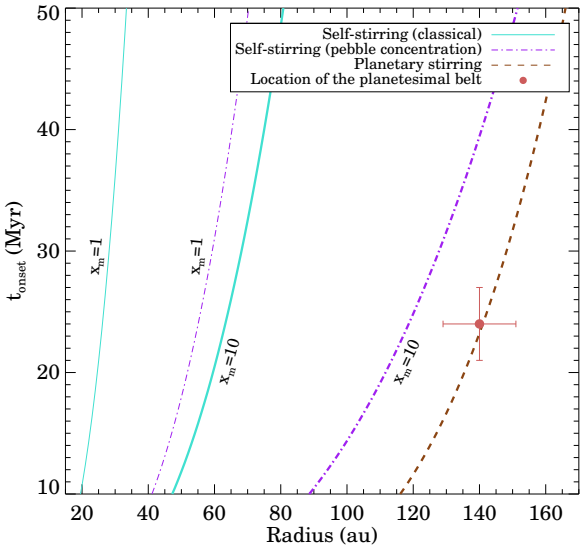

Figure 6. Onset time of the stirring as a function of stellocentric radius for different stirring scenarios (Sect. 4.6). The red dot corresponds to the observed property of the CP−72 2713 system.

alytical formula for the formation time of 1000 km-size planetesimals (the onset time of the stirring) at a stellocentric radius r:

$$t_{\rm onset}^{\rm classical} = 145 x_{\rm m}^{-1.15} \left(\frac{r}{80\,{\rm au}}\right)^{3} \left(\frac{2M_{\odot}}{M_{*}}\right)^{3/2} {\rm Myr}. \quad (4)$$

Realistically, the $x_{\rm m}$ factor could not be higher than 10 (Mustill & Wyatt 2009). Taking a disk with the above-described radial surface density profile with $x_{\rm m} = 10$, and assuming that the location of the planetesimal belt at 140 au in the CP−72 2713 system corresponds to the outer edge of the initial protoplanetary disk, the total initial mass of solids would have been $\sim 1.2\times10^{3}\,{\rm M}_{\oplus}$. This hugely exceeds the measured dust masses of protoplanetary disks around similar mass stars in the Lupus and Chameleon I star forming regions (Ansdell et al. 2016; Pascucci et al. 2016), further confirming the usage of $x_{\rm m} = 10$ as a strong upper limit[5]. In Figure 6 we plot the onset time of the stirring at different radii for $x_{\rm m} = 1$ and $x_{\rm m} = 10$ (solid cyan lines). A comparison with the location of the planetesimal belt in the CP−72 2713 system (red circle), demonstrates that even with $x_{\rm m} = 10$ the radius of the predicted stirring front is very far from the region of the observed planetesimal belt at the age of the system.

[5] We note that Kenyon & Bromley (2008) derived Eq. 4 by fitting their model results for disks with $x_{\rm m}$ values between 1/3 and 3.

The collisional coagulation model is not the sole feasible way for the formation of large planetesimals. Particle concentration models predict a significantly quicker formation of larger bodies even far from the star (at r >100 au) through gravitational collapse of locally concentrated pebbles (Johansen et al. 2015; Krivov & Booth 2018, and references therein). According to these scenarios large planetesimals are already present in the disk by the time of the dissipation of the gas-rich protoplanetary material. Due to the possibly smaller size of the largest bodies (few hundreds kilometers, Simon et al. 2016; Schäfer et al. 2017) with respect to the classical model (where the 1000 km sized planetesimals can stir the neighbouring disk promptly), the excitation of the surrounding smaller bodies takes more time than in the previous scenario. According to Krivov & Booth (2018), in this scenario the onset time of effective self-stirring at a radius r can be computed as

$$t_{\rm onset}^{\rm pebble} = \left(\frac{129}{x_{\rm m}}\right)\left(\frac{1}{\gamma}\right)\left(\frac{\rho}{1{\rm gcm}^{-3}}\right)^{-1}\left(\frac{v_{\rm frag}}{30{\rm ms}^{-1}}\right)^{4} \left(\frac{S_{\rm max}}{200{\rm km}}\right)^{-3}\left(\frac{M_{*}}{M_{\odot}}\right)^{-3/2}\left(\frac{r}{100{\rm au}}\right)^{3}({\rm Myr}), \quad (5)$$

where γ is a parameter in eq. 20 in Krivov & Booth (2018), ρ is the bulk density of planetesimals, $v_{\rm frag}$ is the minimum collisional velocity needed for fragmentation, and $S_{\rm max}$ is the size of the largest planetesimals. Figure 6 shows – by using the default values proposed by Krivov & Booth (2018) of $\gamma = 1.5$, $\rho = 1{\rm gcm}^{-3}$, $v_{\rm frag} = 30{\rm ms}^{-1}$, and $S_{\rm max} = 200$km – that the outer edge of the possibly stirred region (purple dash-dotted line) is close to the position of the planetesimal belt in the CP−72 2713 system. Here we again adopted $x_{\rm m} = 10$. Considering the caveats of the model and the uncertainties of fundamental model parameters (Krivov & Booth 2018), it means that the excitation of CP−72 2713 disk can be consistent with the pebble concentration stirring model. For instance, by adopting somewhat larger maximum planetesimal sizes of $S_{\rm max}$=230 km, the model would predict exactly 24 Myr for the onset of stirring at 140 au, the location of the belt.

Dynamical excitation of a planetesimal disk can also be caused by a planet via its secular perturbation (Wyatt 2005; Mustill & Wyatt 2009). Similarly to the self-stirring scenario, the gravitational influence of a planet located within the planetesimal belt manifests in an outward propagating stirring front. Using the model developed by Mustill & Wyatt (2009) and assuming a Saturn-mass planet with an orbital radius of 65 au (roughly corresponding to the orbital radius of the outermost planet in the HR 8799 system) and a moderate eccentricity of

0.1, we found that the perturbation induced by such a planet could just reach the region of the belt by the age of the system (Fig. 6). The same result can be obtained with a smaller planetary mass if the semimajor axis and/or the eccentricity of the orbit is larger. Thus planetary stirring is a feasible model for the CP−72 2713 system.

Finally, we cannot exclude the possibility that the planetesimal belt is pre-stirred, i.e. born stirred (Wyatt 2008) because of some yet not specified physical mechanism. In this scenario the $t_{\rm onset} = 0$ at all radii.

5. SUMMARY

In this paper we present the results of our multiwavelength observations of a cold debris disk that we discovered around CP−72 2713, a K7/M0-type member of the ∼24 Myr old β Pic moving group. By analyzing the obtained SED we found that the excess spectrum is almost identical to a pure blackbody with a temperature of 43 K and a fractional luminosity of 1.1×10^{-3}. No CO line emission was detected in the disk. The derived dust fractional luminosity is prominently high, we know only four other similarly dust-rich Kuiper-belt analogs within 40 pc of the Sun.

Herschel and ALMA images revealed that the observed emission at 100μm and at 1.3 mm is spatially resolved. Analysis of these data allowed us to explore the basic disk morphology. Based on the derived disk orientation there is no evidence for any significant misaligment between the stellar equator and the disk plane, both are inferred to be inclined by ∼45°. Adopting a symmetric Gaussian radial surface brightness profile, our modelling yields disk radii of 99^{+22}_{-26} au and 140±14 au using the 100μm and 1.3 mm data, respectively. By analyzing the possible dust removal mechanisms and the collisional evolution of the disk using the ACE code, we found that those large grains which dominate the observed millimeter emission are likely not moved away significantly from their birth location and thus trace well the parent planetesimal belt. Smaller grains emitting at 100μm, however, might spread inward if the stellar wind is strong enough, potentially explaining the smaller radius found with *Herschel*.

A planetesimal belt radius of ∼140 au has one of the largest among known debris disks hosted by low mass stars. In our neighbourhood we know only a few protoplanetary disks around 0.5–1.0 $M_\odot$ stars that contains substantial amount of dust material at 140 au, i.e. the location of the planetesimal belt in CP−72 2713. Supposing that this planetesimal belt was already at the same place when it was formed then it could be the offspring of a very extended protoplanetary disk.

We also examined the possible dynamical excitation of the planetesimal belt. By applying different stirring models, we found that the presence of dust producing planetesimals at a radius of ∼140 au is incompatible with the classical self-stirring scenario that assumes slow incremental growth of planetesimals. Stirring by a planet or self-stirring by planetesimals formed rapidly by pebble concentration, however can explain the dust production even in this extended, young disk.

AU Mic and CP−72 2713 both belong to the BPMG suggesting that they were born in the same star forming cloud approximately at the same time. The two systems show further resemblances: their late-type active central stars are surrounded by cold debris disks. Therefore, considering its somewhat more massive host star and more dust-rich and extended debris disk, CP−72 2713 appears to be a massive analog (a big sibling) of AU Mic. Being the first representative of debris disks orbiting a low mass star, AU Mic has been the target of many different studies (e.g. Augereau & Beust 2006; MacGregor et al. 2013; Boccaletti et al. 2015) and played a central role in understanding physical mechanisms that can shape circumstellar material in such systems (Strubbe & Chiang 2006; Schüppler et al. 2015). The disk of CP−72 2713 has a similar angular size to that of AU Mic but it is closer to face-on, which makes it a more favorable target to investigate the spatial structure of debris disks around low luminosity stars.

The authors thank the anonymous referee for their comments and suggestions which helped to improve the paper. This paper makes use of the following ALMA data: ADS/JAO.ALMA#2017.2.00200.S. ALMA is a partnership of ESO (representing its member states), NSF (USA) and NINS (Japan), together with NRC (Canada) and NSC and ASIAA (Taiwan) and KASI (Republic of Korea), in cooperation with the Republic of Chile. The Joint ALMA Observatory is operated by ESO, AUI/NRAO and NAOJ. This work has made use of data from the European Space Agency (ESA) mission *Gaia* (https://www.cosmos.esa.int/gaia), processed by the *Gaia* Data Processing and Analysis Consortium (DPAC, https://www.cosmos.esa.int/web/gaia/dpac/consortium). Funding for the DPAC has been provided by national institutions, in particular the institutions participating in the *Gaia* Multilateral Agreement. This research has made use of the VizieR catalogue access tool, CDS, Strasbourg, France (DOI : 10.26093/cds/vizier). The original description of the VizieR service was published

in A&AS 143, 23. This work was supported by the Hungarian NKFIH grant KH130526.

Facilities: Spitzer, Herschel, ALMA, TESS

Software: CASA (McMullin et al. 2007), uv-multifit (Martí-Vidal et al. 2014), mpfit (Markwardt 2009), MOPEX (MOsaicking and Point source Extraction, Makovoz & Marleau 2005), FLATW'RM code (Vida & Roettenbacher 2018), MUFRAN (Kolláth 1990), Stilism (Capitanio et al. 2017; Lallement et al. 2018)

APPENDIX

A. ANALYSIS OF THE TESS DATA

CP−72 2713 was observed in 2-minute (short) cadence by Camera 3 of *TESS* spacecraft in Sectors 1 (between 2018 July 25 and August 22) and 13 (between 2019 June 19 and July 18). In our analysis we utilized the Simple Aperture Photometry (SAP) light curves that were downloaded from the MAST archive[6]. We removed data points where the quality flags indicated problems using bit-wise AND operation with the binary mask 101010111111 as suggested by the TESS Data Product Overview[7]. Zero-point of TESS magnitude scale (i.e. the magnitude - flux conversion factor) has been set using the GAIA DR2 RP magnitude (Gaia Collaboration et al. 2018), by exploiting the almost complete overlap of the corresponding response functions at the far optical red and near-IR regimes (see fig. 1 in Ricker et al. 2015 and fig. 3 in Jordi et al. 2010). The obtained light curves show a clear periodic modulation likely due to rotation of stellar spots (Fig. 7).

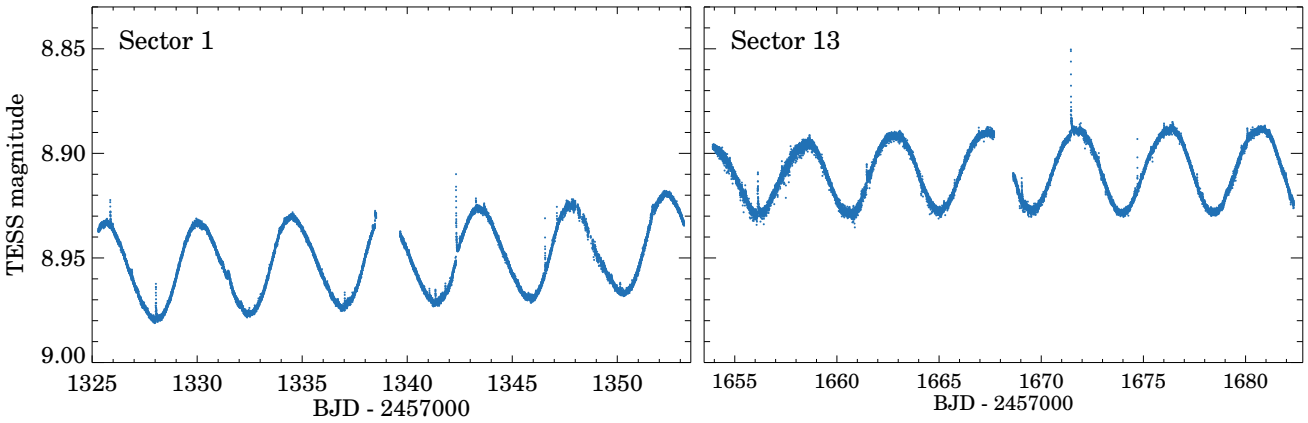

Figure 7. *TESS* short cadence light curves of CP−72 2713 measured a) in Sector 1 and b) in Sector 13.

For the Fourier analysis of the short cadence light curves we subtracted a linear fit from the observations from each sector. Although these could be caused either by real intrinsic changes or instrumental artifacts, due to the distribution of the data points it is not possible to reliably fit variations on this time scale with Fourier components. The remaining data was analyzed using MUFRAN (Kolláth 1990). The main feature in the Fourier-spectrum of the light curve (see Fig. 8) is connected to the rotation ($P = 4.437$ days), the other peaks – an order of magnitude weaker – are either present at the double frequency of this signal, or close to the main rotation period. These latter peaks could be a result of spots located at different latitudes showing a slightly different rotation rate due to differential rotation. A weak trend with the length of approximately the observing runs is also present.

Flares in the light curve were identified using the FLATW'RM code (Vida & Roettenbacher 2018), that uses a machine-learning algorithm to give a robust model of the light curves in order to detect flare events and uses a voting system implemented to keep false positive detections to a minimum. We originally set a 3σ detection limit, that was lowered to 2σ as visual inspection of the results proved that there were no false positives identified. The minimum data points for a flare was set to 3, the degree of polynomials to describe light curves was set to 10. In the light curve

[6] https://mast.stsci.edu
[7] https://outerspace.stsci.edu/display/TESS/2.0+-+Data+Product+Overview

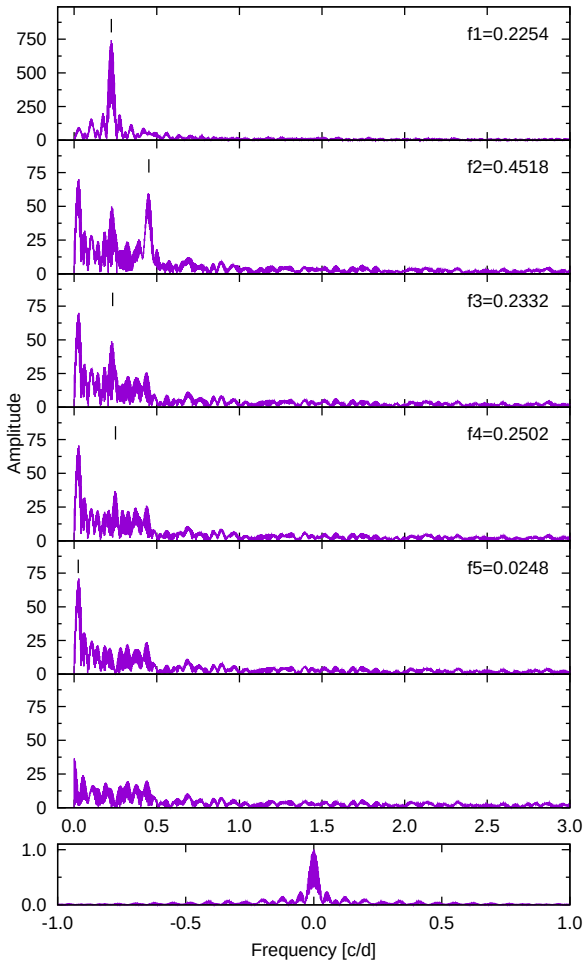

Figure 8. Fourier analysis of the TESS light curve. The upper five panels show the Fourier spectra of the light curve, after pre-whitening with the dominant frequency marked with a dash (note: the top plot has a different y scale). The bottom two panels show the spectral window, and the residual light curve (note: largest flare is cropped), respectively.

51 events were identified: altogether 1.24% of the data was considered part of a flare event. All the eruptions are relatively weak, each has an amplitude < 0.04 magnitudes.

REFERENCES

Andrews, S. M., Wilner, D. J., Hughes, A. M., et al. 2010, ApJ, 723, 1241

Andrews, S. M., Rosenfeld, K. A., Kraus, A. L., et al. 2013, ApJ, 771, 129

Andrews, S. M., Terrell, M., Tripathi, A., et al. 2018, ApJ, 865, 157

Ansdell, M., Williams, J. P., van der Marel, N., et al. 2016, ApJ, 828, 46

Ansdell, M., Williams, J. P., Trapman, L., et al. 2018, ApJ, 859, 21

Augereau, J.-C., & Beust, H. 2006, A&A, 455, 987

Aumann, H. H. 1985, PASP, 97, 885

Bailer-Jones, C. A. L., Rybizki, J., Fouesneau, M., Mantelet, G., & Andrae, R. 2018, AJ, 156, 58

Balog, Z., Müller, T., Nielbock, M., et al. 2014, Experimental Astronomy, 37, 129

Barrado y Navascués, D., & Martín, E. L. 2003, AJ, 126, 2997

Bell, C. P. M., Mamajek, E. E., & Naylor, T. 2015, MNRAS, 454, 593

Boccaletti, A., Thalmann, C., Lagrange, A.-M., et al. 2015, Nature, 526, 230

Bohren, C. F., & Huffman, D. R. 1983, New York: Wiley, 1983
Booth, M., Dent, W. R. F., Jordán, A., et al. 2017, MNRAS, 469, 3200
Burns, J. A., Lamy, P. L., & Soter, S. 1979, Icarus, 40, 1
Campbell, B., & Garrison, R. F. 1985, PASP, 97, 180
Capitanio, L., Lallement, R., Vergely, J. L., Elyajouri, M., & Monreal-Ibero, A. 2017, A&A, 606, A65
Carpenter, J. M., Bouwman, J., Silverstone, M. D., et al. 2008, ApJS, 179, 423
Casey, C. M., Narayanan, D., & Cooray, A. 2014, PhR, 541, 45
Castelli, F., & Kurucz, R. L. 2004, ArXiv Astrophysics e-prints, astro-ph/0405087
Cataldi, G., Brandeker, A., Wu, Y., et al. 2018, ApJ, 861, 72
Chavez-Dagostino, M., Bertone, E., Cruz-Saenz de Miera, F., et al. 2016, MNRAS, 462, 2285
Choi, J., Dotter, A., Conroy, C., et al. 2016, ApJ, 823, 102
Cranmer, S. R., Wilner, D. J., & MacGregor, M. A. 2013, ApJ, 772, 149
Cutri, R. M., & et al. 2013, VizieR Online Data Catalog, 2328,
Daley, C., Hughes, A. M., Carter, E. S., et al. 2019, ApJ, 875, 87
Davenport, J. R. A., Hawley, S. L., Hebb, L., et al. 2014, ApJ, 797, 122
Donaldson, J. K., Roberge, A., Chen, C. H., et al. 2012, ApJ, 753, 147
Dotter, A. 2016, ApJS, 222, 8
Draine, B. T. 2003, ARA&A, 41, 241
Ercolano, B., & Pascucci, I. 2017, Royal Society Open Science, 4, 170114
Faramaz, V., Krist, J., Stapelfeldt, K. R., et al. 2019, AJ, 158, 162
Findeisen, K., Hillenbrand, L., & Soderblom, D. 2011, AJ, 142, 23
Flaherty, K., Hughes, A. M., Mamajek, E. E., & Murphy, S. J. 2019, ApJ, 872, 92
Franco, M., Elbaz, D., Béthermin, M., et al. 2018, A&A, 620, A152
Gagné, J., Mamajek, E. E., Malo, L., et al. 2018, ApJ, 856, 23
Gaia Collaboration, Brown, A. G. A., Vallenari, A., et al. 2018, A&A, 616, A1
Gaidos, E., Mann, A. W., Lépine, S., et al. 2014, MNRAS, 443, 2561
Gáspár, A., Psaltis, D., Rieke, G. H., et al. 2012, ApJ, 754, 74
Geiler, F., Krivov, A. V., Booth, M., et al. 2019, MNRAS, 483, 332
González-López, J., Novak, M., Decarli, R., et al. 2020, arXiv e-prints, arXiv:2002.07199
Gordon, K. D., Engelbracht, C. W., Fadda, D., et al. 2007, PASP, 119, 1019
Goulding, N. T., Barnes, J. R., Pinfield, D. J., et al. 2012, MNRAS, 427, 3358
Greaves, J. S., Kennedy, G. M., Thureau, N., et al. 2014, MNRAS, 438, L31
Günther, M. N., Pozuelos, F. J., Dittmann, J. A., et al. 2019, arXiv:1903.06107
Hendler, N., Pascucci, I., Pinilla, P., et al. 2020, arXiv e-prints, arXiv:2001.02666
Holland, W. S., Matthews, B. C., Kennedy, G. M., et al. 2017, MNRAS, 470, 3606
Huang, J., Andrews, S. M., Dullemond, C. P., et al. 2018, ApJL, 869, L42
Hughes, A. M., Duchêne, G., & Matthews, B. C. 2018, ARA&A, 56, 541
Ishihara, D., Onaka, T., Kataza, H., et al. 2010, A&A, 514, A1
Johansen, A., Mac Low, M.-M., Lacerda, P., et al. 2015, Science Advances, 1, 1500109
Jordi, C., Gebran, M., Carrasco, J. M., et al. 2010, A&A, 523, A48
Kalas, P., Liu, M. C., & Matthews, B. C. 2004, Science, 303, 1990
Kennedy, G. M., Wyatt, M. C., Bryden, G., et al. 2013, MNRAS, 436, 898
Kenyon, S. J., & Bromley, B. C. 2008, ApJS, 179, 451
Kiraga, M. 2012, AcA, 62, 67
Kolláth, Z., Konkoly Observatory Occasional Technical Notes, 1
Kral, Q., Wyatt, M., Carswell, R. F., et al. 2016, MNRAS, 461, 845
Kral, Q., Matrà, L., Wyatt, M. C., & Kennedy, G. M. 2017, MNRAS, 469, 521
Kral, Q., Clarke, C., & Wyatt, M. C. 2018, Handbook of Exoplanets, 165
Kral, Q., Marino, S., Wyatt, M. C., et al. 2019, MNRAS, 489, 3670
Krivov, A. V., Löhne, T., & Sremčević, M. 2006, A&A, 455, 509
Krivov, A. V. 2010, Research in Astronomy and Astrophysics, 10, 383
Krivov, A. V., & Booth, M. 2018, MNRAS, 479, 3300
Krivov, A. V., Ide, A., Löhne, T., et al. 2018, MNRAS, 474, 2564

Lallement, R., Capitanio, L., Ruiz-Dern, L., et al. 2018, A&A, 616, A132
Lee, J., & Song, I. 2018, MNRAS, 475, 2955
Lieman-Sifry, J., Hughes, A. M., Carpenter, J. M., et al. 2016, ApJ, 828, 25
Lindegren, L., Hernández, J., Bombrun, A., et al. 2018, A&A, 616, A2
Liseau, R., Vlemmings, W., Bayo, A., et al. 2015, A&A, 573, L4
Löhne, T., Krivov, A. V., & Rodmann, J. 2008, ApJ, 673, 1123
Löhne, T., Augereau, J.-C., Ertel, S., et al. 2012, A&A, 537, A110
Long, F., Pinilla, P., Herczeg, G. J., et al. 2018, ApJ, 869, 1
Long, F., Herczeg, G. J., Harsono, D., et al. 2019, arXiv:1906.10809
Low, F. J., Smith, P. S., Werner, M., et al. 2005, ApJ, 631, 1170
MacGregor, M. A., Wilner, D. J., Rosenfeld, K. A., et al. 2013, ApJL, 762, L21
MacGregor, M. A., Wilner, D. J., Andrews, S. M., Lestrade, J.-F., & Maddison, S. 2015, ApJ, 809, 47
MacGregor, M. A., Wilner, D. J., Chandler, C., et al. 2016, ApJ, 823, 79
MacGregor, M. A., Weinberger, A. J., Wilner, D. J., Kowalski, A. F., & Cranmer, S. R. 2018, ApJL, 855, L2
MacGregor, M. A., Weinberger, A. J., Hughes, A. M., et al. 2018b, ApJ, 869, 75
Makovoz, D., & Marleau, F. R. 2005, PASP, 117, 1113
Mamajek, E. E., & Hillenbrand, L. A. 2008, ApJ, 687, 1264
Marino, S., Wyatt, M. C., Kennedy, G. M., et al. 2017, MNRAS, 469, 3518
Marino, S., Carpenter, J., Wyatt, M. C., et al. 2018, MNRAS, 479, 5423
Marino, S., Yelverton, B., Booth, M., et al. 2019, MNRAS, 484, 1257
Markwardt, C. B. 2009, in Astronomical Society of the Pacific Conference Series, Vol. 411, Astronomical Data Analysis Software and Systems XVIII, ed. D. A. Bohlender, D. Durand, & P. Dowler, 251
Marshall, J. P., Maddison, S. T., Thilliez, E., et al. 2017, MNRAS, 468, 2719
Martin, D. C., Fanson, J., Schiminovich, D., et al. 2005, ApJL, 619, L1
Martí-Vidal, I., Vlemmings, W. H. T., Muller, S., & Casey, S. 2014, A&A, 563, A136
Mathioudakis, M., & Doyle, J. G. 1991, A&A, 244, 433
Matrà, L., Panić, O., Wyatt, M. C., & Dent, W. R. F. 2015, MNRAS, 447, 3936
Matrà, L., Dent, W. R. F., Wyatt, M. C., et al. 2017b, MNRAS, 464, 1415
Matrà, L., Marino, S., Kennedy, G. M., et al. 2018, ApJ, 859, 72
Matrà, L., Öberg, K. I., Wilner, D. J., Olofsson, J., & Bayo, A. 2019, AJ, 157, 117
Matthews, B. C., Krivov, A. V., Wyatt, M. C., Bryden, G., & Eiroa, C. 2014, Protostars and Planets VI, 521
Matthews, B. C., Kennedy, G., Sibthorpe, B., et al. 2015, ApJ, 811, 100
McMullin, J. P., Waters, B., Schiebel, D., Young, W., & Golap, K. 2007, in Astronomical Society of the Pacific Conference Series, Vol. 376, Astronomical Data Analysis Software and Systems XVI, ed. R. A. Shaw, F. Hill, & D. J. Bell, 127
Messina, S., Desidera, S., Turatto, M., Lanzafame, A. C., & Guinan, E. F. 2010, A&A, 520, A15
Miyake, K., & Nakagawa, Y. 1993, Icarus, 106, 20
Moór, A., Ábrahám, P., Juhász, A., et al. 2011, ApJL, 740, L7
Moór, A., Pascucci, I., Kóspál, Á., et al. 2011, ApJS, 193, 4
Moór, A., Kóspál, Á., Ábrahám, P., et al. 2015, MNRAS, 447, 577
Moór, A., Kóspál, Á., Ábrahám, P., et al. 2016, ApJ, 826, 123
Mustill, A. J., & Wyatt, M. C. 2009, MNRAS, 399, 1403
Negrello, M., Hopwood, R., De Zotti, G., et al. 2010, Science, 330, 800
Negrello, M., Amber, S., Amvrosiadis, A., et al. 2017, MNRAS, 465, 3558
Olofsson, J., van Holstein, R. G., Boccaletti, A., et al. 2018, A&A, 617, A109
Ossenkopf, V., & Henning, T. 1994, A&A, 291, 943
Ott, S. 2010, in Astronomical Society of the Pacific Conference Series, Vol. 434, Astronomical Data Analysis Software and Systems XIX, ed. Y. Mizumoto, K.-I. Morita, & M. Ohishi, 139
Pawellek, N., Moór, A., Pascucci, I., et al. 2019, MNRAS, 487, 5874
Pál, A. 2012, MNRAS, 421, 1825
Pascucci, I., Testi, L., Herczeg, G. J., et al. 2016, ApJ, 831, 125
Pecaut, M. J., & Mamajek, E. E. 2013, ApJS, 208, 9
Plavchan, P., Jura, M., & Lipscy, S. J. 2005, ApJ, 631, 1161
Poglitsch, A., Waelkens, C., Geis, N., et al. 2010, A&A, 518, L2
Rebull, L. M., Stapelfeldt, K. R., Werner, M. W., et al. 2008, ApJ, 681, 1484
Reidemeister, M., Krivov, A. V., Stark, C. C., et al. 2011, A&A, 527, A57

Ricker, G. R., Winn, J. N., Vanderspek, R., et al. 2015, Journal of Astronomical Telescopes, Instruments, and Systems, 1, 014003
Rieke, G. H., Young, E. T., Engelbracht, C. W., et al. 2004, ApJS, 154, 25
Riviere-Marichalar, P., Barrado, D., Montesinos, B., et al. 2014, A&A, 565, A68
Rosenfeld, K. A., Andrews, S. M., Wilner, D. J., Kastner, J. H., & McClure, M. K. 2013, ApJ, 775, 136
Sánchez-Portal, M., Marston, A., Altieri, B., et al. 2014, Experimental Astronomy, 37, 453
Schäfer, U., Yang, C.-C., & Johansen, A. 2017, A&A, 597, A69
Schüppler, C., Löhne, T., Krivov, A. V., et al. 2015, A&A, 581, A97
Simon, J. B., Armitage, P. J., Li, R., et al. 2016, ApJ, 822, 55
Sissa, E., Olofsson, J., Vigan, A., et al. 2018, A&A, 613, L6
Skrutskie, M. F., Cutri, R. M., Stiening, R., et al. 2006, AJ, 131, 1163
Strubbe, L. E., & Chiang, E. I. 2006, ApJ, 648, 652
Su, K. Y. L., MacGregor, M. A., Booth, M., et al. 2017, AJ, 154, 225
Tazzari, M., Testi, L., Natta, A., et al. 2017, A&A, 606, A88
Torres, C. A. O., Quast, G. R., da Silva, L., et al. 2006, A&A, 460, 695
Torres, C. A. O., Quast, G. R., Melo, C. H. F., & Sterzik, M. F. 2008, Young Nearby Loose Associations, in Handbook of Star Forming Regions, Vol. II, ed. B. Reipurth (SanFrancisco, CA: ASP), 757
Tripathi, A., Andrews, S. M., Birnstiel, T., et al. 2017, ApJ, 845, 44
Zuckerman, B., Rhee, J. H., Song, I., & Bessell, M. S. 2011, ApJ, 732, 61
Zuckerman, B. 2019, ApJ, 870, 27
Vida, K., & Roettenbacher, R. M. 2018, A&A, 616, A163
Vieira, J. D., Marrone, D. P., Chapman, S. C., et al. 2013, Nature, 495, 344
Wardlow, J. L., Cooray, A., De Bernardis, F., et al. 2013, ApJ, 762, 59
Wargelin, B. J., & Drake, J. J. 2001, ApJL, 546, L57
Watson, C. A., Littlefair, S. P., Diamond, C., et al. 2011, MNRAS, 413, L71
Weise, P., Launhardt, R., Setiawan, J., & Henning, T. 2010, A&A, 517, A88
Werner, M. W., Roellig, T. L., Low, F. J., et al. 2004, ApJS, 154, 1
White, J. A., Boley, A. C., MacGregor, M. A., et al. 2018, MNRAS, 474, 4500
Williams, J. P., Najita, J., Liu, M. C., et al. 2004, ApJ, 604, 414
Wood, B. E., Müller, H.-R., Zank, G. P., et al. 2002, ApJ, 574, 412
Wright, E. L., Eisenhardt, P. R. M., Mainzer, A. K., et al. 2010, AJ, 140, 1868
Wyatt, M. C. 2005, A&A, 440, 937
Wyatt, M. C. 2008, ARA&A, 46, 339
Wyatt, M. C., Panić, O., Kennedy, G. M., & Matrà, L. 2015, Ap&SS, 357, 103